

Electronic Supplementary Information (ESI)

**A highly asymmetric interfacial superstructure in WC:
Expanding the classic grain boundary segregation and new
complexion theories**

Zhishan Luo, ‡^a Chongze Hu, ‡^{b,c} Lin Xie,^d Hongbo Nie,^e Congying Xiang,^a Xinfu Gu,^f Jiaqing He,^d Wenqing Zhang,^{d,*} Zhiyang Yu,^{a,*} Jian Luo,^{b,c,*}

^a*State Key Laboratory of Photocatalysis on Energy and Environment, College of Chemistry, Fuzhou University, Fuzhou, Fujian 350002, P. R. China. E-mail: yuzyemlab@fzu.edu.cn*

^b*Program of Materials Science and Engineering, University of California San Diego, La Jolla, California 92093, USA*

^c*Department of Nanoengineering, University of California San Diego, La Jolla, California 92093, USA. E-mail: jluo@ucsd.edu*

^d*Department of Physics, Southern University of Science and Technology, Shenzhen, Guangdong 518055, R. R. China*

^e*Xiamen Tungsten Corporation, Xiamen, Fujian 361126, P. R. China*

^f*School of Materials Science and Engineering, University of Science and Technology Beijing, Beijing 100083, P. R. China*

‡ These authors contributed equally.

* Correspondence should be addressed to J.L. (jluo@alum.mit.edu), Z.Y. (yuzyemlab@fzu.edu.cn), and W.Z. (zhangwq@sustc.edu.cn)

Method

1. Sample Preparation

The tungsten carbide (WC) hard metal containing ~0.29 wt% of TiC (as a grain growth inhibitor) and ~10.0 wt% of Co was prepared by a powder metallurgical (PM) process. Specifically, WC, TiC, and Co powders of Fisher particle sizes of 4.0, 1.5, and 0.8 μm , respectively, were used as starting materials. After mixing and milling, these powders were vacuum dried to produce granulated powders. The granulated powders were pressed in a mould under 150 MPa pressure, dewaxed, and subsequently sintered in vacuum at 1450 °C for 1 hour. Finally, the sintered WC hard metal samples were carefully grinded and polished.

2. Aberration-Corrected Scanning Transmission Electron Microscopy (AC STEM)

We used a focus ion beam (FIB) to prepare transmission electron microscopy (TEM) samples. To guarantee high-resolution STEM imaging, the sample thickness was finally thinned to 80 ± 5 nm. All high-angle annular dark field (HAADF) images and atomic-resolution energy dispersive X-ray spectroscopy (EDS) mapping were recorded on a Thermo Fisher Scientific TEM (Themis Z, 300 kV). The collection angle of HAADF imaging was set 60-200 mrad.

3. Electron Backscattered Diffraction (EBSD)

The EBSD technique was employed to determine the grain boundary (GB) character in Ti-doped WC-Co. Fig. S3 or S10 shows a typical map as an example, where both Co and WC are observed. The lines in these maps indicate high-angle GBs with misorientation larger than 15°. The GBs with orientation relationships close ($<10^\circ$) to $(0001) // (01\bar{1}0)$ and $[2\bar{1}\bar{1}0] // [2\bar{1}\bar{1}3]$, which represent 2-3% of the ~1000 GBs examined, are highlighted with red lines in Fig. S3. All near $(0001) // (01\bar{1}0)$ GBs, which represent 8-9% of all GBs, are highlighted with red lines in Fig. S10.

4. The Model for the WC(0001)-WC(01 $\bar{1}$ 0) GB

The construction of the computation model of WC(0001)-WC(01 $\bar{1}$ 0) GB was based on the experimental STEM HAADF images (Fig. S4A), where the green box highlights a coherent match between a $5 \times (01\bar{1}0)$ grain and a $4 \times (0001)$ grain along the direction parallel to GB. According to this feature, we jointed a 5×3 WC(01 $\bar{1}$ 0) orthogonal supercell with lattice parameters $a = 1.222$ nm and $b = 2.037$ nm (upper Fig. S4B) and a 4×4 WC(0001) orthogonal supercell with lattice parameters $a = 1.167$ nm and $b = 2.021$ nm (lower Fig. S4B). In this case, the strain due to the interface mismatch along a and b directions can be reduced to ~ 4.5% and ~0.8%, respectively. The selection is the best choice to satisfy the periodic boundary conditions with the largest unit cell that can be calculated by DFT. To eliminate vacuum effect, we extended both WC(01 $\bar{1}$ 0) and (0001) orthogonal supercells along c direction 3 times. Finally, a large GB structure with 592 atoms was used for first-principles calculations.

We built DFT models to study two types of interfacial segregation structures:

- (1) For the “dilute segregation structure” that is mainly used to calculate the segregation energy, we generally calculate five to ten different configurations by doping a single atom at different sites.
- (2) For the “full segregation structure”, we doped solute atoms at each layer based on

experimentally measured compositional profiles and five possible configurations were considered as the start point. All of them were subjected to DFT structural relaxation. The structure with the lowest energies will be used to perform further structural analysis.

5. DFT Calculations

First-principles DFT calculations were performed by using Vienna *ab initio* Simulations Package (VASP)^{1,2}. The projected-augmented wave (PAW)^{3,4} method was used to solve Kohn-Sham equations, along with standard PAW potentials for the elements W, C, Ti, and Co. Based on the validations for a gamut of DFT functionals with and without vdW corrections, see Table S1, a nonlocal optB86b-vdW⁵ functional was selected for structural optimization of WC GB structures. It has been previously shown that van der Waals (vdW) interactions can alter structural and cohesive properties not only for layered structure^{6,7}, but also for three-dimensional (3D) bulk materials⁸⁻¹⁰. Due to the large crystal structure (592 atoms), the Brillouin-zone integrations were sampled on a Γ -centered $1 \times 1 \times 1$ grid. The kinetic energy cutoff for plane waves was set to 400 eV, the convergence criterion for electronic self-consistency was set to 5×10^{-4} eV, and the “medium” precision setting was used. The lattice parameters of the WC GB structure were kept unchanged and only atomic positions were fully relaxed until the force components on atoms were smaller than 0.02 eV/Å. To isolate the interaction between GBs, the WC slab was terminated with a vacuum region of ~ 12 Å. The GGA+U method with $U = 3.0$ and $J = 1.0$ eV¹¹ were considered for Ti *d* electrons. The spin-polarized effect was also considered for all calculations, and initial magnetic moments were assigned by $3 \mu_B$ and $5 \mu_B$ to Ti and Co elements respectively.

To assess the segregation tendency of Co and Ti, we calculated the segregation energy E_{seg} by using following equation^{12,13}:

$$E_{seg} = (E_{GB}^{doped} - E_{GB}^{undoped}) - (E_{Bulk}^{doped} - E_{Bulk}^{undoped}) \quad (1)$$

where E_{GB}^{doped} , $E_{GB}^{undoped}$, E_{Bulk}^{doped} and $E_{Bulk}^{undoped}$ are the energies of doped GB, clean GB, doped bulk phase and clean bulk phase. This is essentially the energy difference by moving a dopant atom from bulk to a grain boundary (GB) and Eq. (1) can be re-written as:

$$E_{seg} = (E_{Bulk}^{undoped} + E_{GB}^{doped}) - (E_{Bulk}^{doped} + E_{GB}^{undoped}) \quad (2)$$

Thus, the two terms in the above equation have the exact same total stoichiometry so that the calculated segregation energy does not depend on the chemical potentials. This represents the conventional definition of segregation energy when the sizes of the calculation supercells approach infinity. Here, we use separate supercells for the (doped vs. undoped) bulk WC and the GB structure (with four separate DFT calculations in each case) so that the calculated segregation energy is less sensitive to the size effects. Specifically, a $4 \times 4 \times 4$ supercell with 128 atoms in total was used as WC bulk structure. The GB model is discussed above, and 5-10 different segregation sites at each GB layer and bulk structures were taken into account. A stoichiometric substitution is ensured in each calculation of the segregation energy based on Eq. (1) or (2).

With the fully-optimized WC GB structures, the static all-electron calculations were carried out based on Perdew-Burke-Ernzerhof (PBE)¹⁴ exchange-correlation functional in order to calculate the charge density for both valence and core electrons. The default $96 \times 168 \times 294$ FFT-grids were large enough to sample charge density based on the convergence test for a total number of electrons (Fig. S9). The Bader charge analysis¹⁵ was used to calculate charge transfer for dopant Ti and Co atoms with surrounding C atoms. The CHARGMOL code based on the DDEC6 atomic population analysis method¹⁶ was used to calculate the sum of bond ordering (SBO)¹⁷.

Supplementary Discussion:

1. DFT Validation

Various DFT functionals and methods have been tested and the results are shown in Table S2. We found that several semiempirical functionals, such as PBE-D3, TS, and TS+SCS, a nonlocal optB86b-vdW functional, and PBEsol functionals, produced the best agreements with experimental WC lattice parameters a and c . For graphite, our calculations showed that PBE-TS, TS+SCS, optB88, and optB86b functionals have best estimations for the lattice parameters, but PBE and PBEsol functionals significantly overestimate the c parameter (where $c/2$ is the interlayer distance of graphite layers). For body-centered-cubic (BCC) W, the best DFT functionals for structural optimization are PBE-D3, TS+SCS, optB86b, and PBEsol. Overall, the best DFT functionals for WC, C, and W are semiempirical TS+SCS and non-local optB86b-vdW functionals.

To further compare these two functionals, we calculated the enthalpy of formation for WC using $\Delta H = E_{WC} - E_C - E_W$, where E_{WC} , E_C , and E_W are ground-state energies of WC, C, and W, respectively. The calculated ΔH from the optB86b functional is about -41.835 kJ/mol, which agrees well with the experimental value of -41.83 kJ/mol. However, the TS-SCS functional produced 23.305 kJ/mol, which is significantly larger than the experimental value. Therefore, we finally adopted the **nonlocal optB86b-vdW** functional in our DFT calculations.

2. Excess Charge Transfer

The excess charge transfer Δq_{ex} (a quantity to evaluate the charge transfer) was calculated using following equation:

$$\Delta q_{ex} = \frac{(n_{Ti} * \Delta q_{Ti}^{GB} + n_C * \Delta q_C^{GB})_{GB} - (n_{Ti} * \Delta q_{Ti}^{Bulk} + n_C * \Delta q_C^{Bulk})_{Bulk}}{n_{Ti} + n_C} \quad (3)$$

where $n_{Ti(Co)}$ is the number of dopant atom Ti (or Co), $\Delta q_{Ti(Co)}^{GB}$ is the charge transfer of the dopant Ti (Co) in GB, $\Delta q_{Ti(Co)}^{Bulk}$ is the charge transfer of the dopant Ti (Co) in the bulk, and n_C is the number of C coordination near the dopant atom.

Fig. 7SA showed that $L\bar{1}$ and L0 layers had the largest and second largest Δq_{ex} of 0.069 and 0.028 e/atom for Ti (light blue line with circle), corresponding to lowest and second lowest E_{seg} , respectively. This can be explained by the fact that a large charge transfer can prompt the segregation of solute atoms.^{18, 19} For Co segregation, although the largest Δq_{ex} of 0.069 occurred at $L\bar{1}$, this layer did not correspond to the lowest E_{seg} . This is probably because Co has two different coordination environments: one is at $(01\bar{1}0)$ side with the poor-C coordination environment while the other is at (0001) side with a 6-coordinated C environment.

By plotting the relation of E_{seg} as a function of Δq_{ex} (Fig. S7B), it clearly showed that two linear regions (one is from $L\bar{2}$ to L0, and the other is from L1 to L3) had the same tendency that the larger Δq_{ex} pointed to the lower E_{seg} . It is also worth noting that these two linear regions for Ti was very closed to each other, indicating that Ti coordination environments did not change significantly from (0001) side to $(01\bar{1}0)$ side. This observation was consistent with our coordination analysis in Fig. 3D; for example, the coordination environment of Ti at L1 layer was distorted less than that of Co and the corresponding coordination number is only reduced to ~ 5 .

3. Further Discussion of the Generality of Highly Asymmetric Interfacial Superstructures and the Factors Favoring Their Formation

In the main text, we have already discussed the role of different preferred coordination numbers of Ti, W, and Co in promoting the formation of the observed highly asymmetric interfacial superstructure. Here, we further discuss other bonding nature and characters (e.g., metallic vs. covalent, the degree of close packing, and isotropic vs. anisotropy bonding environment) that may favor the formation of asymmetric interfacial superstructures.

Based on molecular-orbital theory, the bonding of transition-metal monocarbides includes a mixture of covalent, ionic, and metallic contributions^{20,21}. Such a complex bonding nature enables a variety of polymorphs. For instance, a carbide with nine or less valence electrons per unit cell (i.e., four for Ti ($3d^24s^2$) and four for C ($2s^22p^2$)) is more likely to form the FCC structure that is more covalent. In contrast, ten or more valence electrons in WC hexagonal structure (i.e. six for W ($5d^46s^2$) and four for C)²² may lead to more metallic (mixed metallic-covalent) bonding, according to the crystal orbital overlap population (COOP) analysis by Hoffman et al.²² Co-based carbides do not follow the same valence electron rule due to complex metal lattices (Co_2C and Co_3C); however, it is likely that seven d valence electrons of Co ($3d^74s^2$) lead to more metallic bonding in Co-based carbides.

Thus, the asymmetric segregation observed in this study can be related to the transition from the strong covalent bonding in Ti-rich $\text{L}\bar{1}$ layer to the mixed metallic-covalent bonding in the W-rich $\text{L}0$ layer, and finally to the strong metallic bonding in Co-rich $\text{L}1$ layer.

Furthermore, Hoffman et al. suggested that bonding in a closed-packed metal is generally isotropic while the bonding in non-closed-packed metal is more anisotropic. This may imply that the bonding in the FCC TiC is relatively isotropic, the bonding in hexagonal WC is intermediate, while the bonding in Co-based carbides is highly anisotropic. This may also contribute the formation of a highly asymmetric Ti/Co/W based interfacial superstructure observed in this study.

Therefore, we suggest that the highly asymmetric segregation and asymmetric interfacial superstructures may exist in other carbides, as well as borides, nitrides, sulfides, and other materials systems, with similar bonding characters (e.g., different preferred coordination numbers, metallic vs. covalent, the degree of close packing, and isotropic vs. anisotropy bonding environment of the two co-dopants and hosting metals). As we have discussed in the main text, we also expect similar highly asymmetric segregation to occur more frequently at mixed GBs with two low-index grain surface terminal planes (e.g., the three $(0001) // (01\bar{1}0)$ GBs observed in this study), but with little (or less) lattice matching between the two abutting grains. Further experiments and modeling studies are needed to confirm these hypothesis.

Table S1. Layer-by-layer compositional profiles (in at. %) for each element measured from the EDS mapping from Layer $L\bar{4}$ to Layer L3. The measured compositional profiles are plotted in Fig. 2B, where the carbon percentages, averaged from the two adjacent layers, are plotted between two metal layers where carbon atoms sit.

Layer Element	$L\bar{4}$	$L\bar{3}$	$L\bar{2}$	$L\bar{1}$	L0	L1	L2	L3
C	50	45	48	46	48	48	52	51
Ti	1	3	6	24	8	2	1	1
Co	3	3	2	5	9	23	9	4
W	46	49	44	25	35	27	38	44

Note: The detailed procedure to quantify the composition is described below. First, we integrated EDS spectra from the EDS maps on each W layers ($L\bar{4}$ to L3). The integration width was set as the half of the interspacing of those layers (centered at the metal positions). Then, standard EDS quantification was proceed using the VeloxTM software of Thermofisher Scientific company. The composition of each layer was calculated and tabulated in Table S1 above. The sum of atom percentages of four elements is exactly 100% at each layer. However, the C composition of each metal layer is an average of the carbon layers above and below, since C atoms sit between the metal layers. Hence, we averaged C compositions of two adjacent metal layers, and plotted the C percentage data points at their actual positions in Fig. 2B.

Table S2. Calculated lattice parameters (a , c), ground-state energies (E), and enthalpy of formation ($-\Delta H$), for the hexagonal WC (space group: $P\bar{6}m2$, No. 187), graphite C (space group: $P6_3/mmc$, No. 194), and BCC-W (space group: $Im\bar{3}m$, No. 229) using various DFT methods, and comparison with experimental data from the Inorganic Crystal Structure Database (ICSD).

DFT functionals	WC				C (Graphite)			W	
	a (Å)	c (Å)	E (eV/Unit)	$-\Delta H$ (KJ/mol)	a (Å)	c (Å)	E (eV/atom)	a (Å)	E (eV/atom)
PBE	2.924	2.849	-22.457	26.002	2.468	8.685	-9.227	3.185	-12.961
PBE-D2	2.870	2.794	-24.567	68.530	2.464	6.421	-9.336	3.122	-14.521
PBE-D3	2.910	2.843	-23.173	27.813	2.467	6.932	-9.308	3.158	-13.577
TS	2.900	2.840	-23.788	30.616	2.462	6.679	-9.354	3.131	-14.117
TS+SCS	2.916	2.840	-23.305	8.231	2.464	6.706	-9.338	3.163	-13.882
revPBE	2.951	2.874	-16.809	20.578	2.478	7.109	-7.521	3.213	-9.074
optPBE	2.934	2.859	-17.956	30.578	2.472	6.826	-7.874	3.193	-9.765
optB88	2.930	2.854	-18.322	34.263	2.466	6.673	-8.020	3.186	-9.947
optB86b	2.916	2.846	-19.007	41.835	2.468	6.631	-8.138	3.171	-10.436
rPW86	2.982	2.896	-16.343	-3.874	2.477	7.037	-7.620	3.246	-8.764
PBEsol	2.902	2.830	-23.908	43.594	2.462	8.602	-9.643	3.155	-13.813
	2.902	2.849 ^a	/	41.83 ^f	2.462	3.354 ^g	/	3.142 ^h	
		2.889						3.165 ⁱ	
Experiment	2.895	2.858 ^c						3.164 ^j	
	2.894	2.827 ^d						3.168 ^k	
	2.885	2.821 ^e						3.165 ^l	

a. ICSD 246149

b. ICSD 246150

c. ICSD 246151

d. ICSD 260168

e. ICSD 260171

f. Experimental free standard formation enthalpy $\Delta G = -10000 + 1.17T \pm 100$ cal/mol.²³ When $T = 0$, $\Delta G = -10$ kcal/mol = -41.83 kJ/mol.

g. X-ray diffraction data for graphite to 20 GPa.²⁴

h. ICSD 167904

i. ICSD 653430

j. ICSD 653431

k. ICSD 653432

l. ICSD 43421

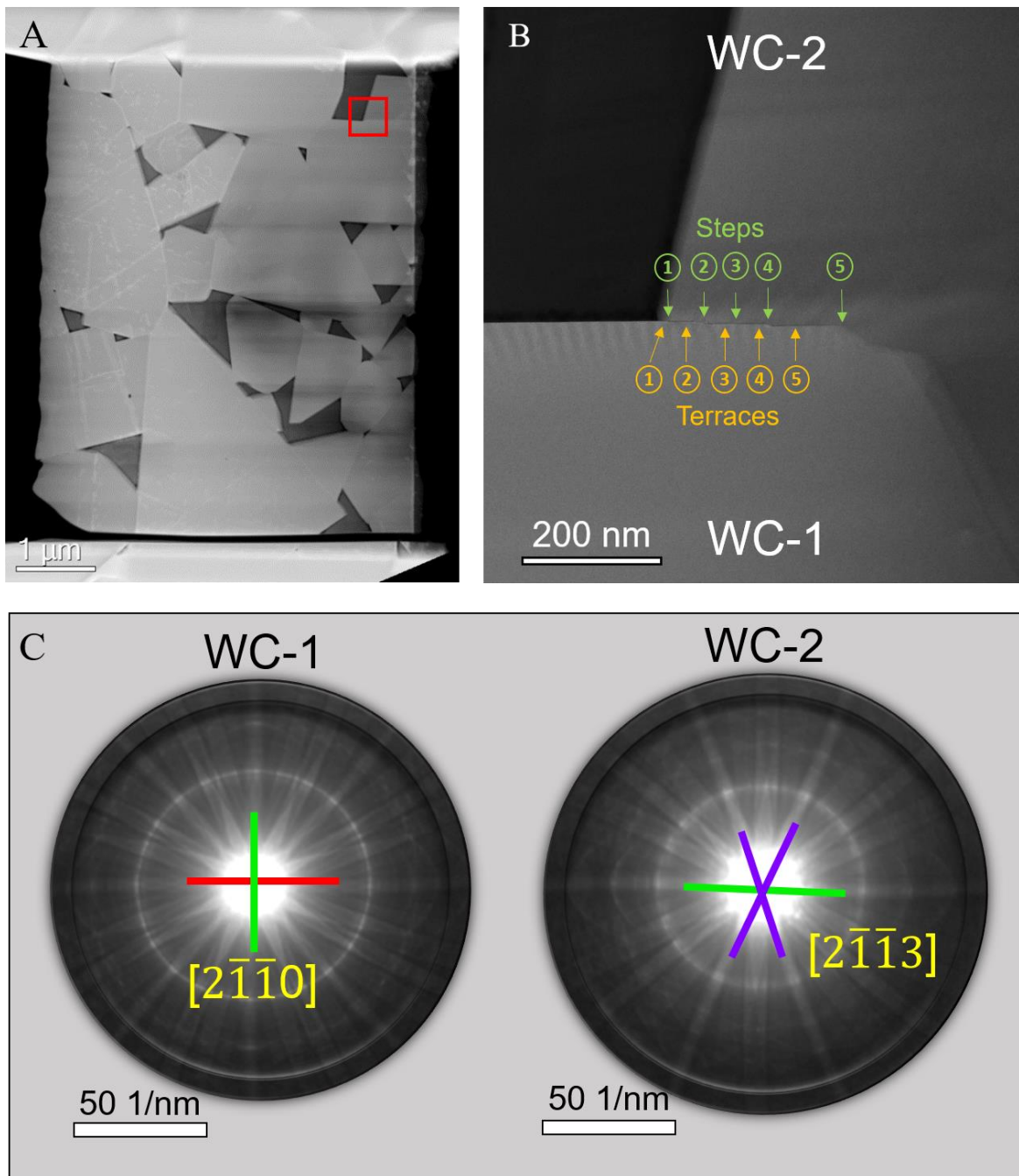


Fig. S1 (A) Microstructure of a Ti-doped WC-Co specimen. The bright crystals are WC grains while the dark regions correspond to the Co phase. No detectable Ti-rich precipitate exists. A $(0001) // (01\bar{1}0)$ and $[2\bar{1}\bar{1}0] // [2\bar{1}\bar{1}3]$ WC GB was found in the right corner of the FIB sample (see the red box). (B) HAADF image of this $(0001) // (01\bar{1}0)$ and $[2\bar{1}\bar{1}0] // [2\bar{1}\bar{1}3]$ WC GB. Wide terraces (numbered in orange) were occasionally interrupted with steps (numbered in green). (C) Kikuchi patterns from the two WC crystals.

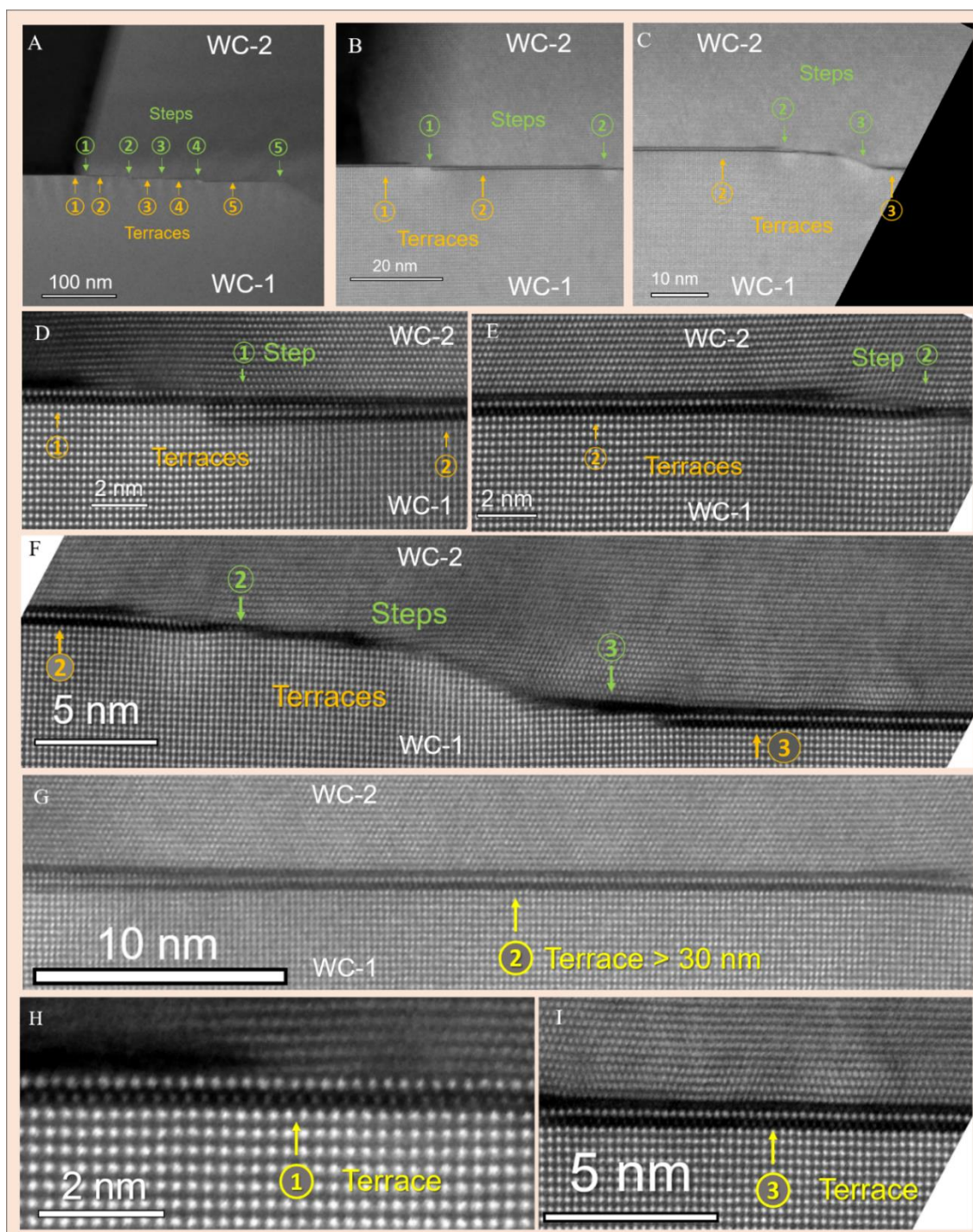


Fig. S2 (A) HAADF image of the $(0001) // (01\bar{1}0)$ and $[2\bar{1}\bar{1}0] // [2\bar{1}\bar{1}3]$ WC GB. Terraces (numbered in orange) are interrupted by several-atom-high steps (numbered in green). (B, C) Low- and (D-F) high-magnification HAADF images of several terraces and steps. (G) The straight Terrace #2 (>30 nm). (H, I) Expanded views of Terraces #1 and #2. Despite that they are interrupted (separated) by steps, the atomically flat segments of the GB exhibit the same structure characterized by the dark/bright/dark fringes, thereby likely representing the equilibrium interfacial structure.

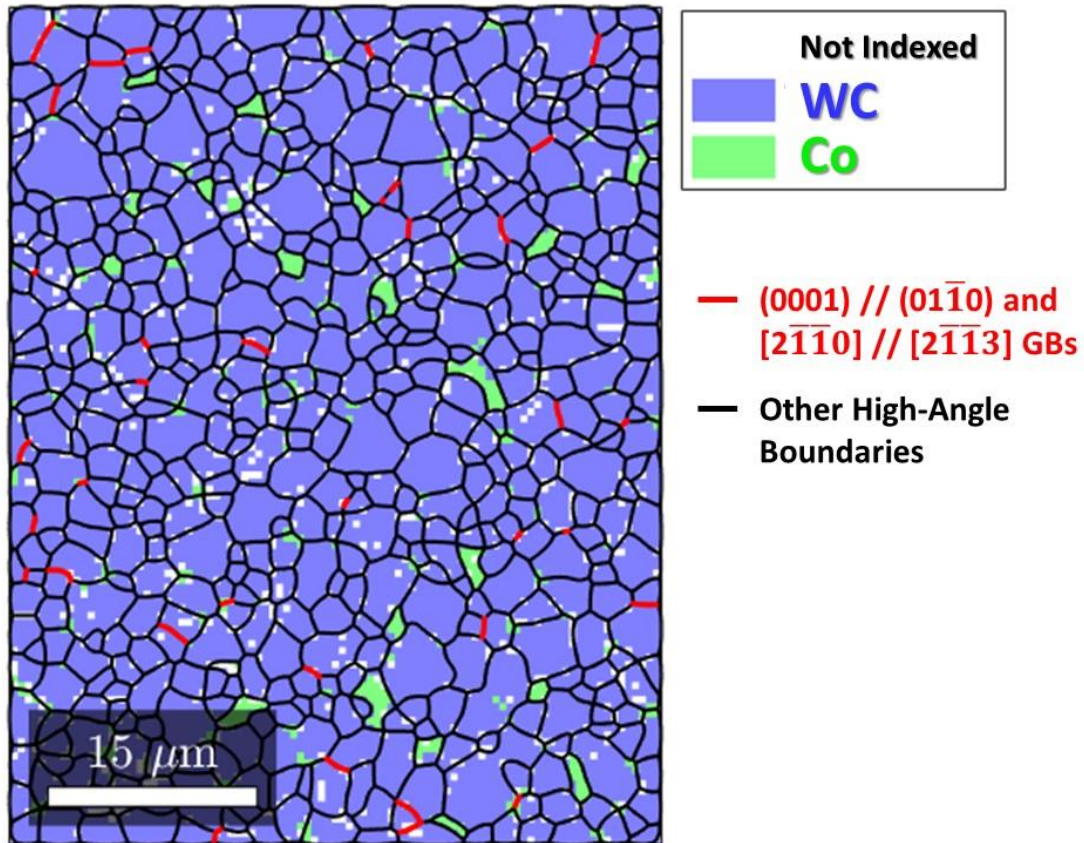


Fig. S3 Electron backscatter diffraction (EBSD) map of the Ti-doped WC-Co. The GBs with characters close to $(0001) // (01\bar{1}0)$ and $[2\bar{1}\bar{1}0] // [2\bar{1}\bar{1}3]$ (i.e., the primary example presented in Fig. 1 and 2 in the main text), which represent ~2-3% of ~1000 GBs examined, are indicated by red lines. Other high-angle boundaries are highlighted by black lines. Noting that all $(0001) // (01\bar{1}0)$ GBs (regardless of the in-plane rotation angles), which represent ~8-9% of all GBs, are indicated in Fig. S10.

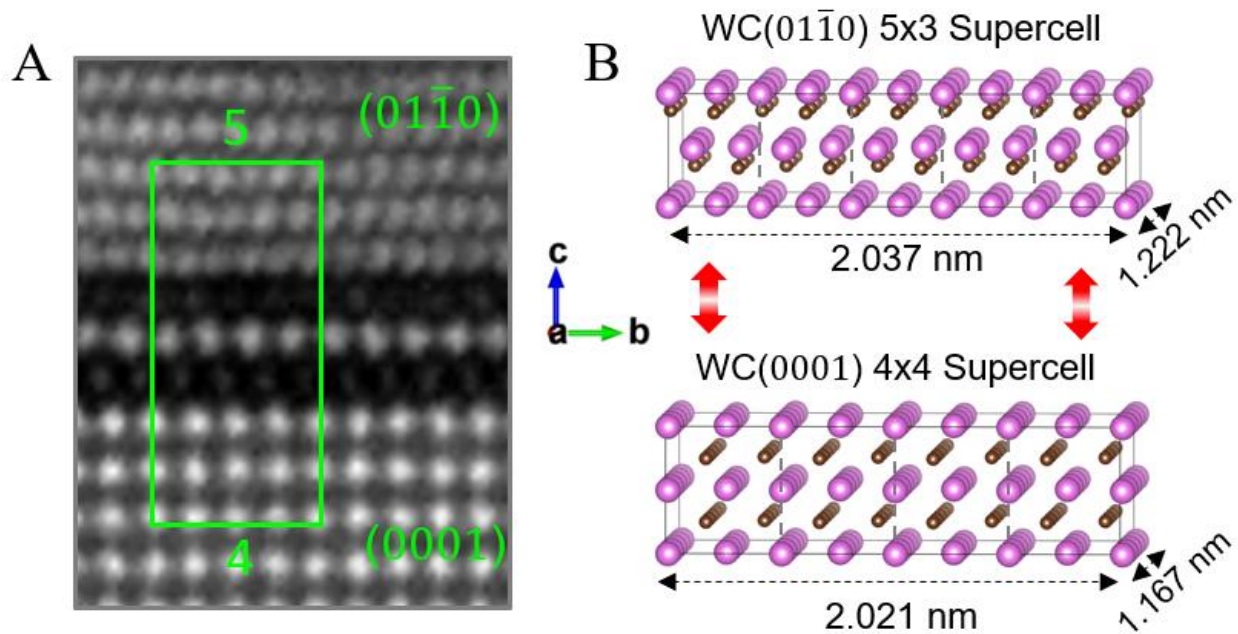


Fig. S4 (A) STEM HAADF image of the WC $(01\bar{1}0) // (0001)$ and $[2\bar{1}\bar{1}3] // [2\bar{1}\bar{1}0]$ GB. The green box highlights a coherent match between $5 \times (01\bar{1}0)$ grains and $4 \times (0001)$ grains along the direction parallel to GB. (B) The computation model of this WC GB jointed by a 5×3 WC $(01\bar{1}0)$ orthogonal supercell and a 4×4 WC (0001) orthogonal supercell.

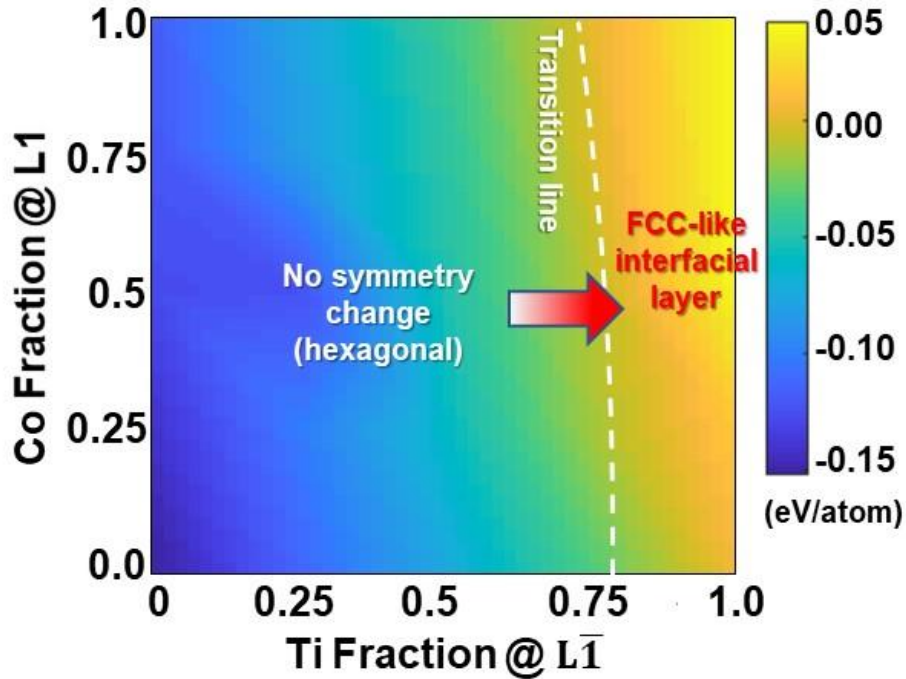


Fig. S5 The GB structure (complexion) stability map as a function of Ti doping fraction at the $L\bar{1}$ layer and Co doping fraction at the L1 layer (on the metal basis, excluding C). The color map represents the calculated energy difference, $\Delta E = (E_{\text{FCC-like}} - E_{\text{no FCC-like}})/N_{\text{atom}}$, where $E_{\text{FCC-like}}$ is the energy of a GB with the formation of an FCC-like layer, $E_{\text{no FCC-like}}$ is the energy of a GB without the symmetry change (i.e., remaining hexagonal without the formation of the FCC-like interfacial layer), and N_{atom} is the total number of atoms. The white dashed line indicates the occurrence of an interfacial structural transition to form an FCC-like interfacial layer with a local (interfacial) symmetry change.

Note: While this result qualitatively shows that the formation of the FCC-like layer is mainly driven by Ti segregation, we note some quantitative discrepancy in the exact concentration threshold for the occurrence of this transition (as the FCC-like interfacial layer forms at a lower Ti fraction in experiments). We believe that this quantitative discrepancy may be resulted from some of the following reasons:

- To calculate Fig. S5, we only doped Ti atoms at the L1 layer, while some Ti atoms also segregated in the L0 layer in experiments, which may prompt the formation of an FCC-like interfacial layer.
- DFT calculation was conducted for 0K, while the experimental structure formed at a high temperature.
- Since we must consider periodic boundary conditions in DFT, there is a strain effect due to the mismatch, which may be relaxed in experiments by the formation of steps (or disconnections); see, e.g., Fig. 1B.

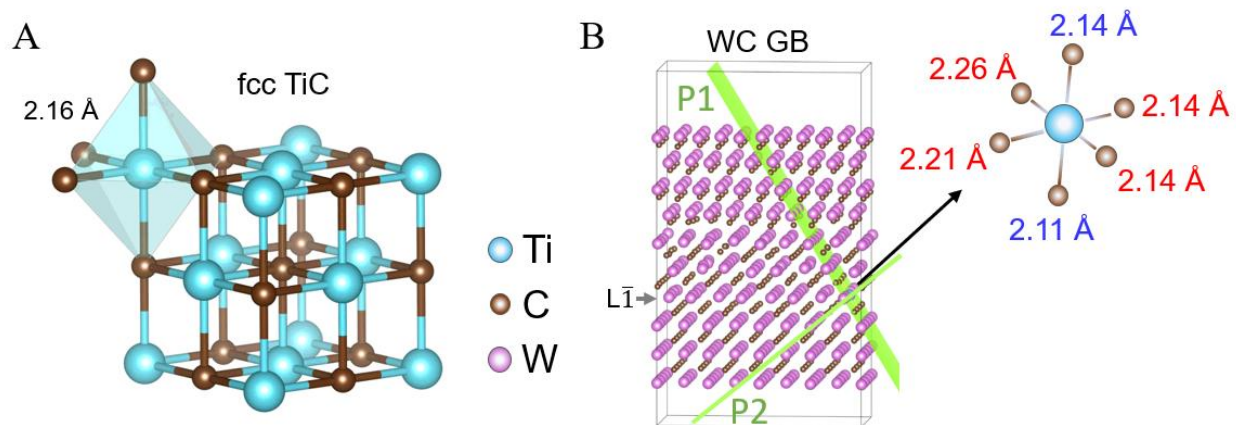


Fig. S6 Crystal structure of (A) rocksalt (FCC) TiC. The Ti atom is octahedrally coordinated with six C atoms, as illustrated by the blue octahedron. The Ti-C bond length is 2.16 Å. (B) DFT-optimized TiC-based, FCC-like interfacial layer formed at the WC GB on the (0001) side (i.e., around the $L\bar{1}$). The four DFT-optimized bond lengths colored in red are on Plane 1 (P1), and the other two colored blue are on Plane 2 (P2). The slightly different bond lengths show there are distortions in the FCC-like interfacial layer (so that it is not a perfect FCC or rocksalt structure).

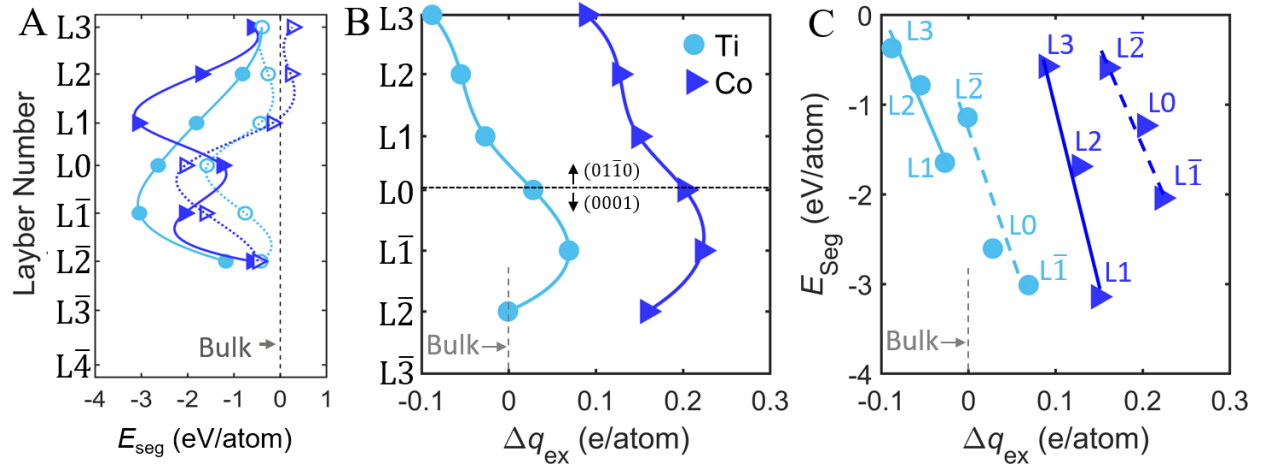


Fig. S7 (A) DFT calculated segregation energies of Ti and Co at different layers, referenced to the bulk. The dashed lines represent the segregation energies without the formation of the FCC-like interfacial layer. (B) Computed excess charge transfer Δq_{ex} of dopant Ti or Co at the different layer position in the direction perpendicular to the WC GB. The black horizontal dot line separates GB into two regions: the upper $(01\bar{1}0)$ side vs. the lower (0001) side. The grey vertical dashed line indicates the computed charge transfer inside the bulk WC grain. (C) Computed segregation energy of dopant atoms as a function of Δq_{ex} . The solid trend lines are drawn for the segregation of Ti and Co at the $(01\bar{1}0)$ side, while the dashed trend lines are drawn for the segregation of Ti and Co at the (0001) side.

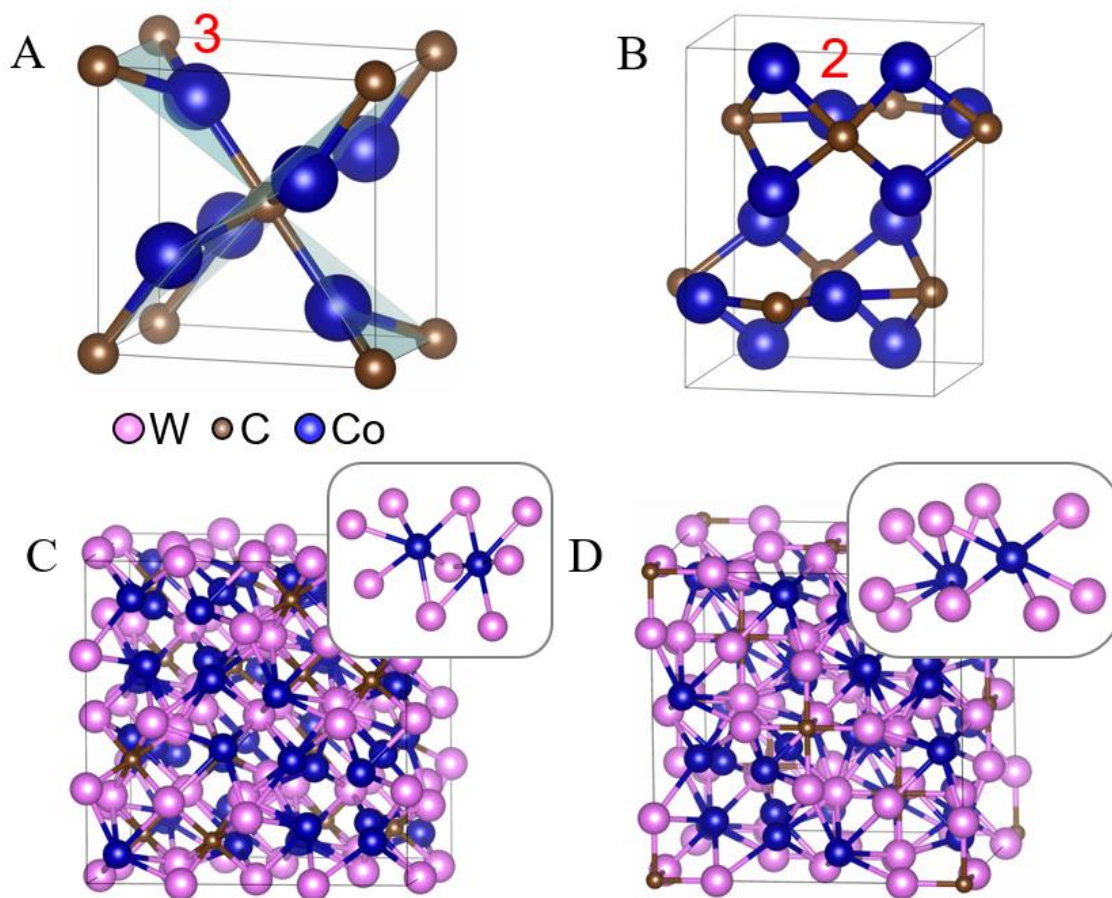


Fig. S8 Crystal structure of DFT-optimized unit cells of **(A)** Co_2C (where the Co atom has a tetrahedral coordination environment with 3 coordinated C), **(B)** Co_3C (where Co only has 2 coordinated C atoms), **(C)** $\text{Co}_3\text{W}_3\text{C}$, and **(D)** $\text{Co}_6\text{W}_6\text{C}$. The insets in panels (C) and (D) are the expanded view of the Co atoms with the bonded W atoms.

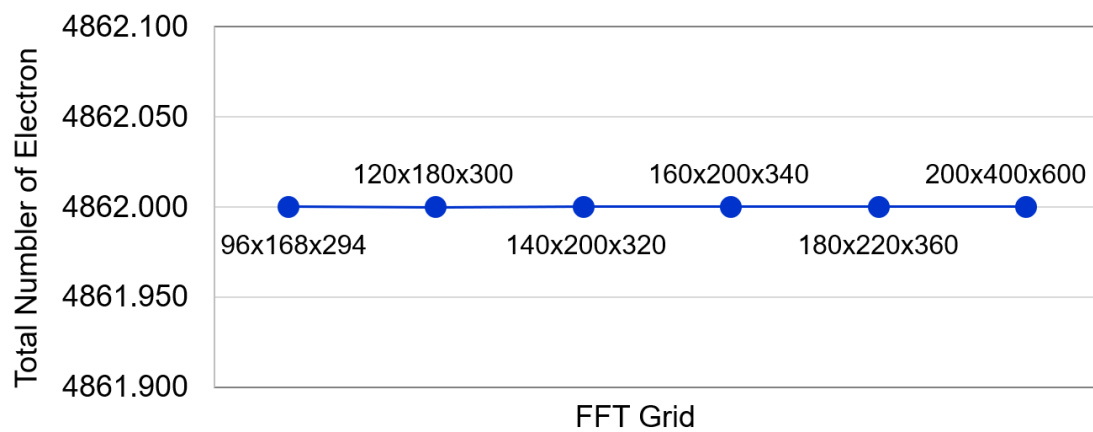


Fig. S9 A convergence test of the FFT grids for computing total number of electrons in the Ti-doped WC GB.

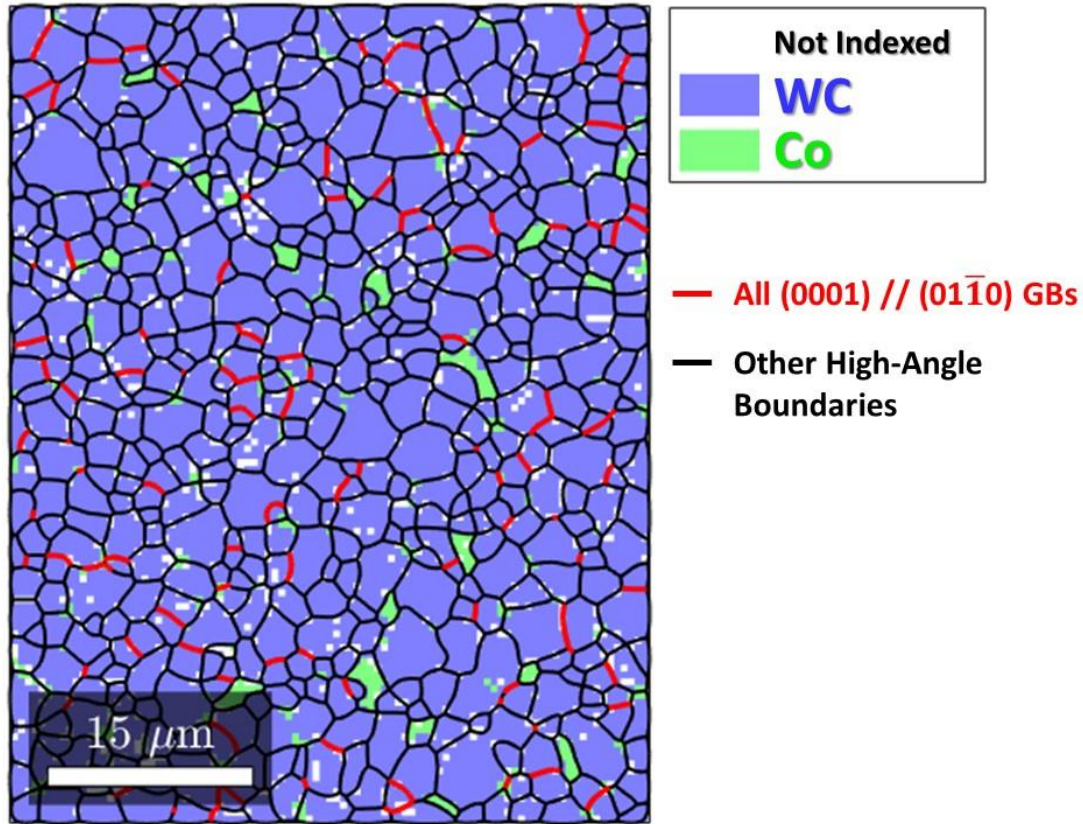


Fig. S10 EBSD map of the Ti-doped WC-Co. All GBs with characters close to $(0001) // (01\bar{1}0)$ (regardless of the in-plane rotation angles), which represent ~8-9% of the ~1000 GBs examined, are shown by red lines. Other high-angle boundaries are highlighted by black lines. Noting that the specific $(0001) // (01\bar{1}0)$ GBs with in-plane rotation close to $[2\bar{1}\bar{1}0] // [2\bar{1}\bar{1}3]$ (similar to the one shown in Fig. 1 and 2 in the main text), represent ~2-3% of all GBs (being a subset of all $(0001) // (01\bar{1}0)$ GBs shown here) and are indicated in Fig. S3. Two additional examples of other $(0001) // (01\bar{1}0)$ GBs are given in Figs. S11 and S12. Altogether, we have examined three $(0001) // (01\bar{1}0)$ GBs, all three exhibit similar interfacial structures (as shown in Figs. S2, S11, and S12).

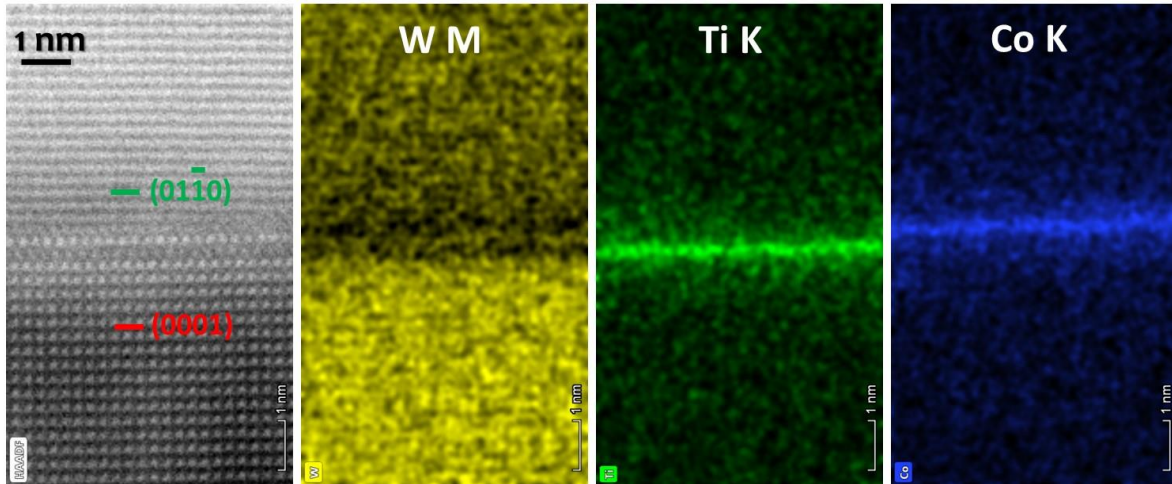


Fig. S11 A second case of a general $(0001) // (01\bar{1}0)$ GB with similar dark/bright/dark fringes in the boundary core. EDS maps of Ti, W and Co indicate that a Ti-rich layer is observed on the (0001) side, while a Co-rich is evident on the $(01\bar{1}0)$ side. Moreover, these two layers are separated by an intermediate W-rich layer, similar to the example shown in Fig. 1 and Fig. 2 in the main text, as well as Fig. S2.

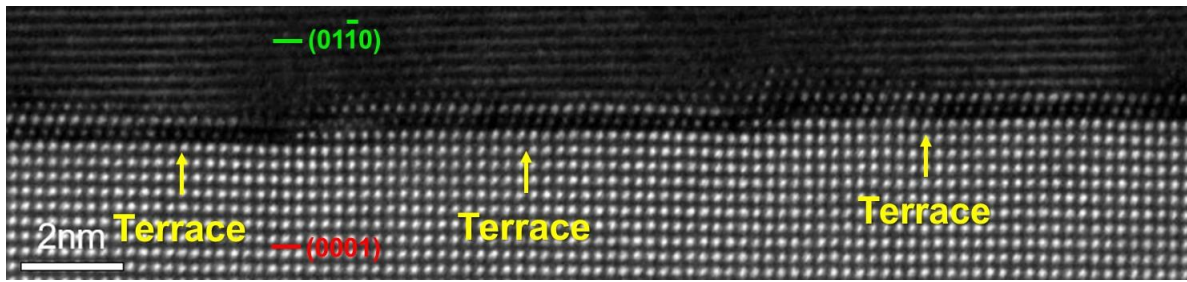


Fig. S12 A third case of a general $(0001) // (01\bar{1}0)$ GB with similar dark/bright/dark structure within discrete terraces that are separated by steps.

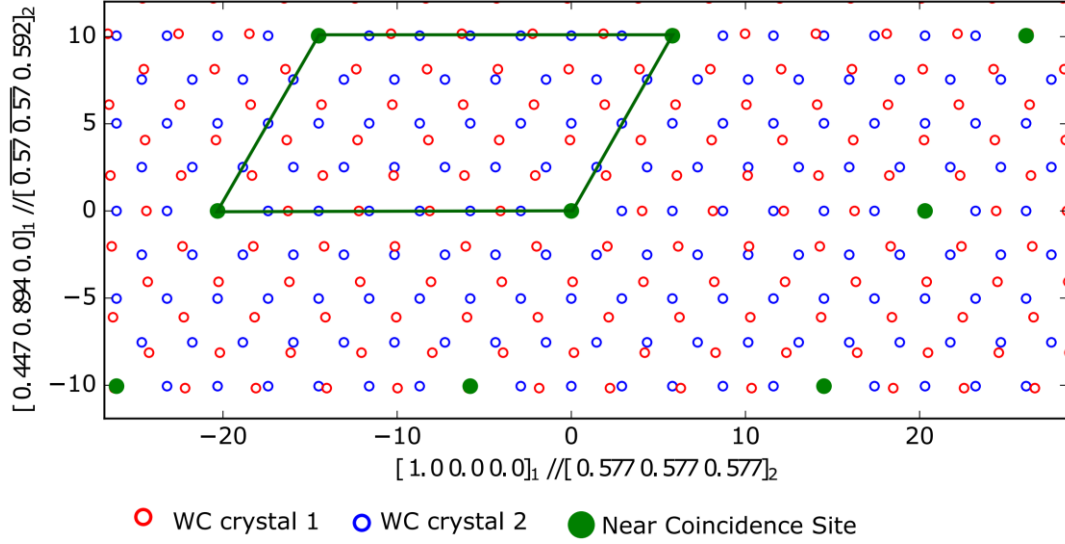


Fig. S13 A crystallography analysis based on Kikuchi patterns (Fig. S1C) shows that this $(0001)_1 // (01\bar{1}0)_2$ and $[2\bar{1}\bar{1}0]_1 // [2\bar{1}\bar{1}3]_2$ WC GB is a “near $\Sigma 28$ ” GB. Here, the Σ value is not exact, but based on a near-coincident cell theory of Bonnet et al.²⁵ for hexagonal crystals (where approximate even Σ values are allowed). To evaluate the sigma value in the WC system, we can plot the near-coincident cell above. Here, the two crystal grains of WC-1 and WC-2 are superimposed at the orientational relationship observed in our study. The near-coincident sites in the interface $(0001)_1 // \{1\bar{1}00\}_2$ are shown as green solid circles, while the lattices for WC-1 and WC-2 are indicated by open red and blue circles respectively. This near-coincident supercell in each lattice are denoted as M1 and M2 respectively; thus, the Sigma value Σ_1 or Σ_2 could be determined by the ratio of size of supercell M1 or M2 to the unit cell in each lattice. They correspond to $\Sigma_1 = 25$ or $\Sigma_2 = 28$ in our case. Thus, this is determined to be a “near $\Sigma 28$ ” GB. Noting that this near-coincident cell theory of Bonnet et al.²⁵ for hexagonal crystals is different from the widely-used theory for cubic crystals, where the sigma values could only be odd numbers.

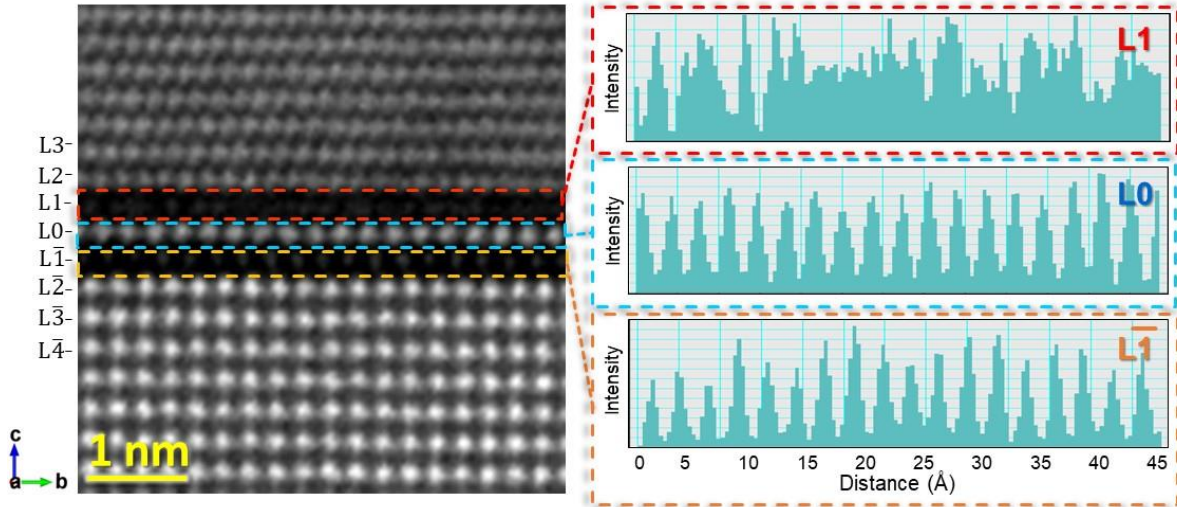


Fig. S14 Illustration and analysis of partial disorder in the segregated Co layer at L1 from experiments. The intensity of HAADF image along b (horizontal) direction of the partially disordered L1 layer vs. the ordered L0 and L1 layers in the (0001) // (0110) and $[2\bar{1}\bar{1}0]$ // $[2\bar{1}\bar{1}3]$ WC GB. The intensity peaks of the L1 layer are non-periodic and largely disordered.

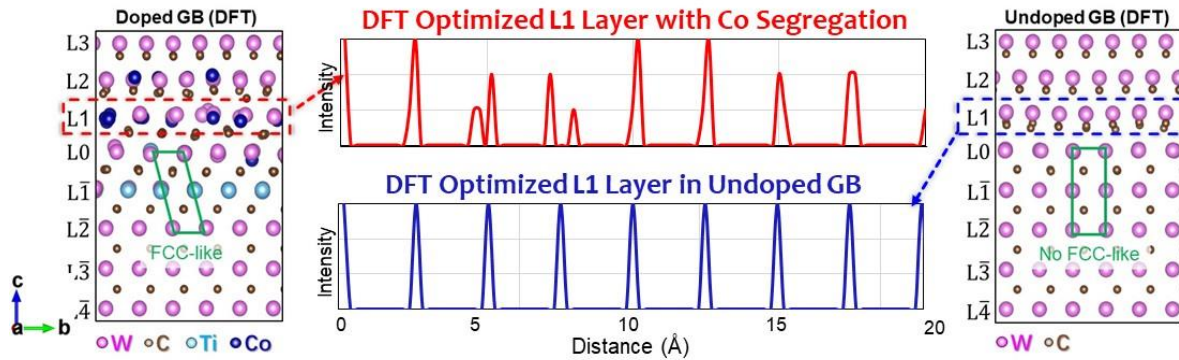


Fig. S15 Illustration and analyses of partial disorder in the segregated Co layer at L1 from the DFT relaxed structures. The effective atomic densities projected along b direction of the L1 layer for the DFT optimized doped and undoped GB structures. The intensity peaks of the L1 layer of the undoped GB are highly ordered and periodic, but they become largely disordered and non-periodic with Co segregation. Both structures were ordered before the DFT relaxations. This comparison suggests that Co segregation induces disordering in the L1 layer, which supports the experimental observation shown in Fig. S14.

Supplementary References:

1. G. Kresse and J. Hafner, *Phys. Rev. B*, 1993, **47**, 558.
2. G. Kresse and J. Furthmuller, *Phys. Rev. B*, 1996, **54**, 11169.
3. P. E. Blochl, *Phys. Rev. B*, 1994, **50**, 17953.
4. G. Kresse and D. Joubert, *Phys. Rev. B*, 1999, **59**, 1758.
5. J. Klimeš, D. R. Bowler and A. Michaelides, *J. Phys.: Conden. Matt.*, 2009, **22**, 022201.
6. Y.-H. Tian, J. Huang, X. Sheng, B. G. Sumpter, M. Yoon and M. Kertesz, *Nano. lett.*, 2015, **15**, 5482–5491.
7. S. Lebègue, J. Harl, T. Gould, J. G. Ángyán, G. Kresse and J. F. Dobson, *Phys. Rev. Lett.*, 2010, **105**, 196401.
8. C. Hu, X. Zeng, Y. Liu, M. Zhou, H. Zhao, T. M. Tritt, J. He, J. Jakowski, P. R. C. Kent, J. Huang and B. G. Sumpter, *Phys. Rev. B*, 2017, **95**, 165204.
9. T. Bučko, S. Lebègue, J. Hafner and J. G. Ángyán, *Phys. Rev. B*, 2013, **87**, 064110.
10. C. Hu, P. Ni, L. Zhan, H. Zhao, J. He, T. M. Tritt, J. Huang and B. G. Sumpter, *Rare Metal*, 2018, **37**, 316-325.
11. Z. Wang, M. Saito, K. P. McKenna, L. Gu, S. Tsukimoto, A. L. Shluger and Y. Ikuhara, *Nature*, 2011, **479**, 380-383.
12. R. Tran, Z. Xu, N. Zhou, B. Radhakrishnan, J. Luo, S. P. Ong, *Acta Mater.*, 2016, **117**, 91-99.
13. S. Yang, N. Zhou, H. Zheng, S. Y. Ong and J. Luo, *Phys. Rev. Lett.*, 2018, **120**, 085702.
14. J. P. Perdew, K. Burke and M. Ernzerhof, *Phys. Rev. Lett.*, 1996, **77**, 3865.
15. G. Henkelman, A. Arnaldsson and H. Jonsson, *Compt. Mater. Sci.*, 2006, **36**, 354-360.
16. T. A. Manz and N. G. Limas, *RSC Adv.*, 2016, **6**, 47771-47801.
17. N. G. Limas and T. A. Manz, *RSC Adv.*, 2018, **5**, 2678-2707
18. C. Hu and J. Luo, *Script. Mater.*, 2019, **158**, 11-15.
19. H. Zheng, R. Tran, X.-G. Li, B. Radhakrishnan and S. P. Ong, *Acta Mater.*, 2018, **145**, 470-476.
20. C. Hu, J. Huang, B. G. Sumpter, E. Meletis and T. Dumitrică, *ACS Appl. Nano. Mater.*, 2018, **1**, 2029-2035.
21. Z. Wu, X.-J. Chen, V. V. Struzhkin and R. E. Cohen, *Phys. Rev. B*, 2005, **71**, 214103.
22. S. D. Wijeyesekera and R. Hoffmann, *Organometallics*, 1984, **3**, 949-961.
23. D. K. Gupta and L. L. Seigle, *Metall. Trans. A*, 1975, 6A, 1940-1944.
24. Y. X. Zhao and I. L. Spain, *Phys. Rev. B*, 1989, **40**, 993.
25. R. Bonnet, E. Cousineau and D. H. Warrington, *Acta Cryst.*, 1981, **A37**, 184–189.